

The First Release of the AST3-1 Point Source Catalogue from Dome A, Antarctica

Bin Ma,^{1,2,3} Zhaohui Shang,^{4,1,2*} Yi Hu,^{1,2} Keliang Hu,¹ Qiang Liu,¹ Michael C. B. Ashley,⁵ Xiangqun Cui,^{6,2} Fujia Du,^{6,2} Dongwei Fan,¹ Longlong Feng,⁷ Fang Huang,⁸ Bozhong Gu,^{6,2} Boliang He,¹ Tuo Ji,⁹ Xiaoyan Li,^{6,2} Zhengyang Li,^{6,2} Huigen Liu,¹⁰ Qiguo Tian,⁹ Charling Tao,^{11,12} Daxing Wang,⁶ Lifan Wang,^{7,13,2} Songhu Wang,¹⁴† Xiaofeng Wang,¹² Peng Wei,¹⁰ Jianghua Wu,⁸ Lingzhe Xu,⁶ Shihai Yang,^{6,2} Ming Yang,¹⁰ Yi Yang,^{8,13,15} Ce Yu,¹⁶ Xiangyan Yuan,^{6,2} Hongyan Zhou,⁹ Hui Zhang,¹⁰ Xueguang Zhang,⁷ Yi Zhang,⁶ Cheng Zhao,^{12,1} Jilin Zhou,¹⁰ Zong-Hong Zhu⁸

¹National Astronomical Observatories, Chinese Academy of Sciences, Beijing 100012, China

²Chinese Center for Antarctic Astronomy, Nanjing 210008, China

³School of Astronomy and Space Science, University of Chinese Academy of Sciences, Beijing 100049, China

⁴Tianjin Astrophysics Center, Tianjin Normal University, Tianjin 300387, China

⁵School of Physics, University of New South Wales, NSW 2052, Australia

⁶Nanjing Institute of Astronomical Optics and Technology, Nanjing 210042, China

⁷Purple Mountain Observatory, Nanjing 210008, China

⁸Department of Astronomy, Beijing Normal University, Beijing 100875, China

⁹Polar Research Institute of China, 451 Jinqiao Rd, Shanghai 200136, China

¹⁰School of Astronomy and Space Science and Key Laboratory of Modern Astronomy and Astrophysics in Ministry of Education, Nanjing University, Nanjing 210093, China

¹¹Aix Marseille Univ, CNRS/IN2P3, CPPM, Marseille, France

¹²Physics Department and Tsinghua Center for Astrophysics (THCA), Tsinghua University, Beijing, 100084, China

¹³George P. and Cynthia Woods Mitchell Institute for Fundamental Physics & Astronomy, Texas A. & M. University, Department of Physics and Astronomy, 4242 TAMU, College Station, TX 77843, USA

¹⁴Department of Astronomy, Yale University, New Haven, CT 06511, USA

¹⁵Department of Particle Physics and Astrophysics, Weizmann Institute of Science, Rehovot 76100, Israel

¹⁶Tianjin University, Tianjin 300072, China

Accepted XXX. Received YYY; in original form ZZZ

ABSTRACT

The three Antarctic Survey Telescopes (AST3) aim to carry out time domain imaging survey at Dome A, Antarctica. The first of the three telescopes (AST3-1) was successfully deployed on January 2012. AST3-1 is a 500 mm aperture modified Schmidt telescope with a 680 mm diameter primary mirror. AST3-1 is equipped with a SDSS *i* filter and a 10k × 10k frame transfer CCD camera, reduced to 5k × 10k by electronic shuttering, resulting in a 4.3 deg² field-of-view. To verify the capability of AST3-1 for a variety of science goals, extensive commissioning was carried out between March and May 2012. The commissioning included a survey covering 2000 deg² as well as the entire Large and Small Magellanic Clouds. Frequent repeated images were made of the center of the Large Magellanic Cloud, a selected exoplanet transit field, and fields including some Wolf-Rayet stars. Here we present the data reduction and photometric measurements of the point sources observed by AST3-1. We have achieved

* E-mail: zshang@gmail.com

† 51 Pegasi b Fellow

a survey depth of 19.3 mag in 60 s exposures with 5 mmag precision in the light curves of bright stars. The facility achieves sub-mmag photometric precision under stable survey conditions, approaching its photon noise limit. These results demonstrate that AST3-1 at Dome A is extraordinarily competitive in time-domain astronomy, including both quick searches for faint transients and the detection of tiny transit signals.

Key words: techniques: image processing – methods: observational – methods: data analysis

1 INTRODUCTION

Small aperture telescopes with wide fields-of-view (FoV) have long played a prominent role in time-domain astronomy. Numerous projects have achieved significant success in searching for rare transient events, such as near-Earth asteroids (NEAs), Potentially Hazardous Asteroids (PHAs), supernovae (SNe), gamma-ray bursts (GRBs) and tidal disruption events (TDEs), e.g., PTF (Law et al. 2009) and Pan-STARRS (Kaiser et al. 2002; Chambers et al. 2016). The photometric monitoring of large sky areas also provides very valuable data sets for variability studies of stars and active galactic nuclei (AGN).

Bellm (2016) compares the survey capabilities of existing and planned projects, among which telescopes with a diameter less than one meter are also competitive. The Catalina Real-time Transient Survey (CRTS, Drake et al. 2009) has repeatedly scanned the sky for nearly a decade and detected thousands of SNe. Many areas of astronomy have benefited from such a dataset of long-term light curves, e.g., the finding of a possible supermassive black-hole binary in a quasar (Graham et al. 2015). The All Sky Automated Survey for SuperNovae (ASAS-SN, Shappee et al. 2014), deploys telescopes with 14-cm aperture lenses, and has discovered more than 500 bright SNe since 2013, including the most luminous SN candidate ever found (Dong et al. 2016; Godoy-Rivera et al. 2017; however, Leloudas et al. 2016 and Margutti et al. 2017 suggest it is a TDE event). Recently, there has been growing interest to develop transient surveys using 50-cm class telescopes. In Hawaii, the Asteroid Terrestrial-impact Last Alert System (ATLAS, Tonry 2011; Tonry et al. 2018) consists of two 50-cm telescopes with 30 deg² FoVs. ATLAS automatically scans the entire accessible sky several times every night. A major science goal of ATLAS is to look for moving objects and provide warnings for killer asteroids. Since its first light in June 2015, ATLAS has discovered 127 NEAs, 17 PHAs, 9 comets, as well as more than one thousand SNe¹. Meanwhile in La Silla, Chile, in the southern hemisphere, blackGEM (Bloemen et al. 2016) is under construction. In Phase 1, it will be an array of three 65-cm telescopes, each with 2.7 deg² FoV. In Phase 2, blackGEM is proposed to be extended to 15 identical telescopes. Although ATLAS and blackGEM are equipped with the same CCD cameras, ATLAS has a pixel scale of 1''86 to maximize its FoV, while blackGEM has a pixel scale of 0''56 to obtain seeing-limited image quality and to push the survey depth down to $g \sim 22$.

Most ground-based transit surveys utilize small tele-

scopes (aperture sizes around 20 cm) to search for exoplanets. Examples include WASP (Pollacco et al. 2006), HATNET (Bakos et al. 2004) and HATSouth (Bakos et al. 2013). By surveying large areas of the sky to milli-mag (mmag) precision with rapid cadence, these surveys have discovered a number of exoplanets. Recently, the ongoing Next Generation Transit Survey (NGTS, Chazelas et al. 2012; Wheatley et al. 2017) has employed an array of twelve 20 cm telescopes to find transiting Neptunes and super-Earths.

Near continuous monitoring of the sky enables comprehensive and rapid detections of transient phenomena that are intrinsically variable on short timescales. Studies of stellar variability also benefit from the long-term continuous photometry that probes a wide range of frequencies. For the highest-quality and most continuous datasets, a good site is essential. The Antarctic Plateau has long been known as a premier astronomical site since its atmosphere is extremely cold, dry, tenuous, and stable (Saunders et al. 2009). Thus it is favorable for optical, infrared and THz observations. In particular, the decreased high-altitude turbulence above the plateau results in reduced scintillation noise (Kenyon et al. 2006) thereby improving photometric and astrometric performance. The polar night in Antarctica provides the opportunity for continuous observations of up to months, uninterrupted by the diurnal cycle at temperate sites. Moreover, Lawrence et al. (2004) reported a mean seeing of 0''27 (median 0''23) at Dome C above a low boundary layer (Bonner et al. 2010), drawing the attention of astronomers worldwide.

In 2005, the 21st CHInese National Antarctic Research Expedition (CHINARE) arrived at Dome A, the highest location of Antarctic plateau, for the first time. Since then Chinese astronomers have conducted site testing campaigns at Dome A in partnership with international collaborators. The results from various facilities have revealed that Dome A has an atmospheric boundary layer as thin as 14 m (Bonner et al. 2010), a strong temperature inversion above the snow surface but low wind speed (Hu et al. 2014), low water vapor (Shi et al. 2016), low sky brightness and low cloud fraction (Zou et al. 2010; Yang et al. 2017). In addition to site testing, the first generation telescope, Chinese Small Telescope ARray (CSTAR, Yuan et al. 2008; Zhou et al. 2010), continuously monitored an area of 20 deg² centered at the South Celestial Pole for three winters beginning in 2008. The photometric precision from CSTAR reached 4 mmag after various efforts to correct the inhomogeneous effect of clouds (Wang et al. 2012), ghost images (Meng et al. 2013) and diurnal effects (Wang et al. 2014a). CSTAR produced many studies of variable stars and exoplanets (e.g. Wang et al. 2011; Yang et al. 2015; Wang et al. 2015; Zong et al. 2015; Oelkers et al. 2016; Liang et al. 2016; Wang et al. 2014b).

Following CSTAR, the Antarctic Survey Telescopes

¹ <http://www.fallingstar.com/home.php>

(AST3) were conceived as the second-generation optical telescopes at Dome A, and designed for multi-band wide-field surveys, with each telescope operating with a different fixed filter. The AST3 telescopes would not only have larger apertures than CSTAR but would also have full pointing and tracking functions. The first and the second AST3—AST3-1 & AST3-2—were installed at Dome A in 2012 and 2015 respectively by the 28th and 31st CHINAREs. The third telescope, AST3-3, is under construction and will be equipped with a K_{dark} -band near-IR camera (Burton et al. 2016; Li et al. 2016).

Here we present the first data release (DR1) of photometric products from AST3-1 in 2012. These data have been used for a study of variable stars in one of the fields (Wang et al. 2017). We organize the paper as follows: the telescope and CCD camera are introduced in §2, the observations are described in §3, the data reduction in §4, we present the photometric results in §5 and summarize the paper in §6.

2 AST3-1

The AST3-1 telescope, built by the Nanjing Institute of Astronomical Optics & Technology (NIAOT), has a modified Schmidt system design (Yuan & Su 2012). It has an entrance pupil diameter of 500 mm, a primary mirror diameter of 680 mm, a focal ratio of $f/3.73$ and a large FoV with a diameter of $\sim 3^\circ$. The main features of AST3-1 include good image quality, a planar focal plane, reduced atmospheric dispersion, an absence of distortion and a compact structure. In the r - or i -bands, 80 per cent of the light energy of a point source is encircled within $1''$. The largest distortion across the FOV is 0.012 per cent, i.e. roughly $1''$ across the 3° diameter. The tube is about half the length of a traditional Schmidt telescope. Unlike CSTAR, AST3-1 has full pointing and tracking components, as well as a focusing system. AST3-1 is powered by the PLATEau Observatory for Dome A² (PLATO-A, Ashley et al. 2010). As an evolution of the original PLATO, PLATO-A is a self-contained automated platform for supplying power of 1 kW continuously for a year, with Internet access provide by Iridium satellites.

AST3-1 is equipped with an SDSS i filter and the CCD camera is designed and manufactured by Semiconductor Technology Associates, Inc.. The CCD has 10560×10560 pixels with a pixel size of $9 \mu\text{m}$, corresponding to $1''$ in the focal plane of AST3. To avoid the possible malfunction of a mechanical shutter, frame transfer mode was adopted to terminate the exposure. To do so, the CCD is divided into two parts with equal area: the frame store regions and the exposure area, giving an effective FoV of $2.93^\circ \times 1.47^\circ$, or $\sim 4.3 \text{ deg}^2$. There are 16 individual readout amplifiers to accelerate the readout, which takes 40 s in slow mode (100 kHz), or 2.5 s in fast mode (1.6 MHz). The CCD chip is cooled by a thermoelectric cooler (TEC) and takes advantage of the low ambient air temperature at Dome A, which is about -60°C on average in winter (Hu et al. 2014). Detailed lab tests of the camera have been performed by Ma et al. 2012, including linearity, the photon transfer curve, readout noise, dark current level and charge transfer efficiency. For example, the

readout noise is $11 e^-$ in fast mode and is reduced to $4 e^-$ in slow mode. The camera was equipped with an engineering-grade CCD with many defective pixels and nearly half the area in one of the sixteen channels was damaged, resulting in an overall 3 per cent loss in effective FoV.

The hardware and software for the operation, control and data (COD) system were developed by the National Astronomical Observatories, Chinese Academy of Sciences (NAOC) (Shang et al. 2012; Hu et al. 2016, Shang et al. in preparation). The highly customized hardware consists of main control, disk array and pipeline computers. Each computer is duplicated to provide redundancy in order to minimize single points of failures. Attention to reliability was essential since the system has to run unattended during the observing season in austral winter. In order to ensure successful observations, we have overcome various technical difficulties encountered specifically in Antarctica. We have developed customized, stable, powerful but low power consumption computers and data storage arrays able to work in the harsh environment. Additionally, the software suite includes an automatic survey control, a scheduler (Liu et al. 2018), a data storage system, a real-time data processing pipeline and a robust photometry database system. The processing must be done on-site since the available Internet bandwidth, and the data communication costs, prohibited bringing back more than a tiny fraction of the data in real-time.

3 OBSERVATIONS IN 2012 AT DOME A

The first AST3 (AST3-1) was deployed to Dome A, Antarctica by the 28th CHINARE team in January 2012 (Li et al. 2012) and became the largest optical telescope in Antarctica. Installed during the bright sunshine of the polar day, AST3-1 had to wait for operation until mid-March when twilight began. After tests of focusing, pointing and tracking, the telescope began commissioning observations. Unfortunately the telescope stopped working on May 8 due to a malfunction in the power supply system. During the March to May period, two major observing modes—the survey mode and the monitoring mode—were performed to verify the performance of the telescope and CCD camera. In survey mode, the footprint covered roughly $2,000 \text{ deg}^2$ with 496 fields. The exposure time of each image was 60 s and in total more than 3,000 images were obtained. The images were used as reference templates for searching for SNe and other transients; we refer to this as the SN Survey. The telescope also surveyed 50 fields covering the Large Magellanic Cloud (LMC) and 12 fields covering the Small Magellanic Cloud (SMC). Fig. 1 shows the sky coverage of the survey mode. In a separate “monitoring mode”, each of several fields were monitored for hours. The monitored fields include the center of LMC, a transit field where the exoplanets OGLE-TR-111b, 113b and 132b are located, as well as the Wolf-Rayet stars HD 117688, HD 136488, HD 143414 and HD 88500. In addition to the surveys, AST3-1 observed many other targets such as stellar cluster, galaxies, quasars and follow-ups of SNe and GRBs. Since these observations did not have many repeated exposures of the same fields, we do not include these data here. Observation statistics for the survey and monitoring modes are shown in Table 1 and Table 2, respectively.

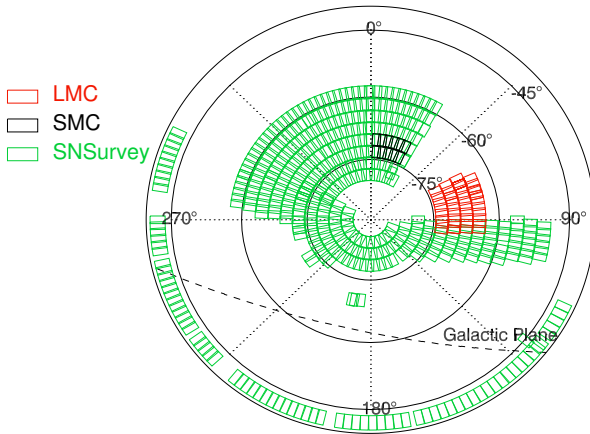
² <http://mcba11.phys.unsw.edu.au/~plato-a>

Table 1. Statistics of the AST3-1 survey mode observations in 2012

| Object | No. of fields | Sky coverage (deg ²) | No. of frames | Total exposure time (hr) | No. of sources detected |
|-----------|---------------|----------------------------------|---------------|--------------------------|-------------------------|
| LMC | 50 | 200 | 664 | 10.60 | 3,038,210 |
| SMC | 12 | 50 | 55 | 0.9 | 227,608 |
| SN Survey | 496 | 2000 | 3084 | 51.4 | 12,768,876 |

Table 2. Statistics of the AST3-1 monitoring mode observations in 2012

| Object | RA (deg) | DEC (deg) | No. of frames | Total exposure time (hr) | No. of light curves |
|------------|----------|-----------|---------------|--------------------------|---------------------|
| LMC-center | 80.894 | -69.756 | 4183 | 58.6 | 815,589 |
| Transit | 163.9 | -61.5 | 3158 | 35.0 | 764,279 |
| HD117688 | 203.3755 | -62.317 | 655 | 5.0 | 137,206 |
| HD136488 | 231.0471 | -61.6771 | 660 | 4.2 | 148,798 |
| HD143414 | 240.9557 | -62.6933 | 1442 | 7.6 | 66,284 |
| HD88500 | 152.633 | -60.6451 | 591 | 2.2 | 41,578 |

**Figure 1.** The sky coverage of survey observations from AST3-1 in 2012. The small boxes denote the size and shape of the AST3 FoV while the colours indicate different surveys according to the legend. The dashed line is the Galactic Plane.

AST3-1 was commissioned in unmanned operating mode at one of the most remote sites on Earth, and with extreme site conditions. Non-negligible instrumental effects needed to be modeled to process the data effectively. The main issue was the irregular point spread function (PSF) resulting from significant tube seeing caused by the heat from the camera and the unstable tracking of AST3-1. As seen in Fig. 2, the full-width at half-maximum (FWHM) of the stellar images varied from 2'' to 6'' with a median of roughly 4''. The profiles of stars were elongated when unstable tracking occurred. The elongation, defined as the ratio of semi-major to semi-minor axis, had a median of 1.09 but exceeded 1.2 in some cases. There was also a polar misalignment of about 0.7° due to difficulties such as limited working time, manpower and resources at Dome A, while performing the installation process during daytime. The pointing accuracy

was improved to $\sim 2'$ after TPoint correction³ was applied to compensate for polar misalignment.

4 DATA REDUCTION

The raw data from AST3-1 were retrieved by the 29th CHINARE team in 2013. The preliminary reduction of the raw science images involved corrections for CCD cross-talk, over-scan, dark current and flat-fielding. Fig. 3 illustrates an example of the reduction of a raw image in the Transit field. We then performed photometry on the preprocessed images and applied flux and astrometric calibrations on the extracted source catalogs. Light curves were built by cross-matching catalogues in the same field. Each step is detailed in the respective subsection below, particularly for custom methods used to derive the dark current and in constructing the flat-field.

4.1 CCD cross-talk

CCD cross-talk can occur when multiple outputs from the CCD are read out simultaneously. If one amplifier reads a saturated pixel, the pixels that are read simultaneously by the other amplifiers are influenced. This effect appears as ghosts in the image and can be either positive or negative depending on the CCDs. Since there are sixteen readout amplifiers in AST3-1's CCD camera, the cross-talk effect is significant. Each saturated star results in fifteen negative ghosts in other readout regions and the stars that overlap these ghosts appear darkened. To correct for this effect, we compared the values between the ghosts and their surrounding pixels and derived a uniform cross-talk coefficient $CT = 1.3 \times 10^{-3}$. Then for each readout, we search for every

³ <http://www.tpointsw.uk/>

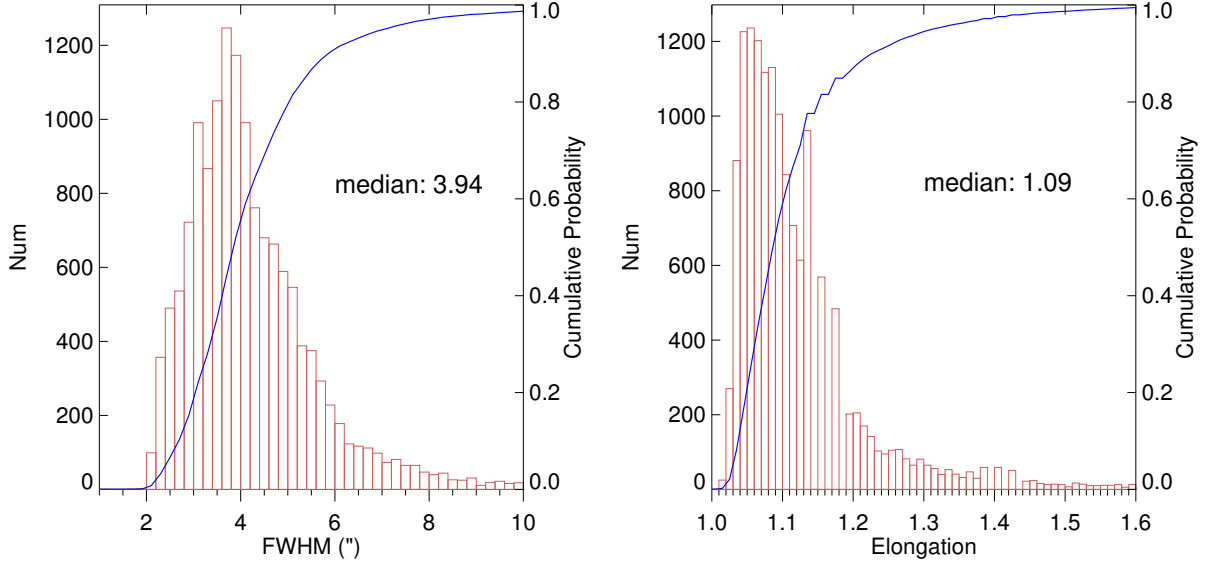


Figure 2. Statistics for the image quality of the AST3-1 2012 commissioning observations. Left panel: FWHM and right panel: elongation.

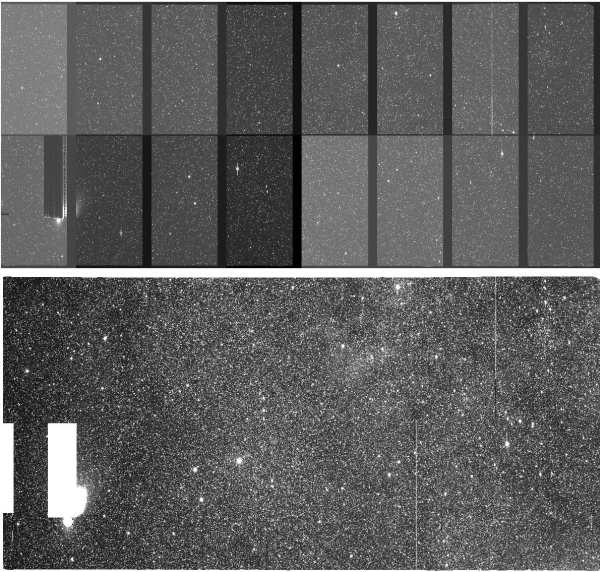


Figure 3. Upper: an example of a raw frame from the Transit field where 16 readouts are obvious due to differing bias levels and over-scan. Lower: the preprocessed image from this example; two white regions in the left-lower readout mask the damaged part of CCD.

saturated pixel and add $65535 \times CT \sim 85$ ADU to the corresponding pixels at the same physical location in the other fifteen readouts.

4.2 Over-scan

Since AST3-1’s camera has no mechanical shutter, even a 0 s exposure is exposed during the frame transfer period, which takes 434 ms, and consequently cannot be used as a bias frame. Therefore, the median of over-scan columns on

each readout was subtracted to remove the consequences of any voltage variations.

4.3 Dark current

Dark currents in the AST3-1 camera were significantly high due to the heat dissipation from the CCD, which had a median temperature of -46°C . While the dark current level is less than the sky brightness, the dark current non-uniformity can exceed the photon noise from the sky background. For example, the image a0331.116.fit taken at $t_{\text{CCD}} = -40^\circ\text{C}$ has a median background of 620 ADU. The RMS of the background is 55 ADU, which is roughly three times the photon shot noise (19 ADU). Therefore it is critical to correct the dark current. However, dark frames could not be obtained during the observing season because of the shutterless camera and the unattended site in winter. We developed a simple but effective method to derive the dark current frame from the scientific images (Ma et al. 2014). Here we briefly describe this method.

The intensity I of a pixel (x, y) can be written as:

$$I(x, y) = S + D(T) + \Delta d(T, x, y), \quad (1)$$

where S is the sky background, $D(T)$ is the median dark current level over the entire CCD at temperature T , and $\Delta d(T, x, y)$ is the deviation from the median dark current at pixel (x, y) . The stars are ignored because they can be removed by a median algorithm when combining a large number of images from various fields. The sky brightness is adequately flat spatially after twilight (Yang et al. 2017) and therefore is taken as a constant. In Eq. 1 the sum of the first two position-independent terms S and $D(T)$ is practically the median value of the full image I_0 . We denote the later term as a fluctuation term, which describes the temperature and position-dependent effect of dark current. Considering two

images taken with the same exposure time and temperature T_0 , the sky brightnesses will in general be different. Recall Eq. 1, the two images have different position-independent terms but the same position-dependent term:

$$\begin{aligned} I_1(x, y) &= I_{0,1} + \Delta d(T, x, y), \\ I_2(x, y) &= I_{0,2} + \Delta d(T, x, y). \end{aligned} \quad (2)$$

Supposing $I_{0,2}$ is brighter, $I_1(x, y)$ can be scaled to the equivalent median level of $I_{0,2}$ by multiplying by the ratio $k \equiv I_{0,2}/I_{0,1}$:

$$I'_1(x, y) = kI_1(x, y) = I_{0,2} + k\Delta d(T, x, y). \quad (3)$$

Subtracting $I_2(x, y)$ from $I'_1(x, y)$ removes the constant term and leaves only the fluctuation term. Consequently the non-uniformity of dark current at temperature T can be calculated from the image pair:

$$\Delta d(T, x, y) = \frac{I'_1(x, y) - I_2(x, y)}{k - 1} = \frac{kI_1(x, y) - I_2(x, y)}{k - 1}. \quad (4)$$

Adding the space-varying term $\Delta d(T, x, y)$ to the median level $D(T)$, we can derive the dark frame at temperature T_0 and exposure time t_0 . Before applying the dark correction, the dark frame needs to be scaled to match the temperature and exposure time of the scientific images. However, it is insufficiently accurate to interpolate via the relationship between dark current level and temperature or time. Instead we use the dark current level of warm pixels as the scale parameter—these are high enough for precision determination and have an identical response to temperature and time as normal pixels.

This technique for correcting for dark-current non-uniformity has proved to be sufficiently robust. For the example above, the background RMS is reduced to 25 ADU, which pushes the limiting magnitude 1 mag deeper.

4.4 Flat-fielding

We constructed a master flat-field frame by median-combining numerous twilight frames. However, the brightness of the twilight sky is not uniform, and the gradient varies with the Sun elevation and angular distance to the Sun. Therefore, the varying gradients in individual twilight frames will introduce systematic uncertainty in the median-combined frame. We correct for the brightness gradient following the method discussed by [Wei et al. \(2014\)](#).

AST3-1 obtained a total of 2,451 twilight frames during its 2012 observations. We selected the images that had adequate sky intensity but were still within the linearity range of the CCD, i.e., between 15,000 and 30,000 ADU. We discarded images taken with CCD temperatures above -40°C , leaving a total of 906 twilight images for further analysis. These frames were then median-combined to generate an initial master flat-field. Each twilight image was then divided by this master flat-field to remove gain variation and vignetting, yielding a relative gradient map to the initial master flat-field. We then fitted each gradient map with a two-dimensional inclined plane $Z = a + bX + cY$. By rejecting images which had a large gradient or large fitting residuals,

we obtained the final sample of 200 images. Before recombining them, we removed the gradients by dividing then by their linear fitting plane. This process was repeated for each readout separately rather than for the full frame, since a nonlinear gradient variation was observed across the entire frame.

Finally, we combined the gradient-corrected images to obtain the final master flat-field. To compare the quality of the initial and final versions, we constructed the RMS image of two samples. The initial RMS map showed a four-times increase from the center to the edge, while the final RMS map exhibits a rather uniform value across the entire frame at a level of 0.1 per cent. The accuracy of this flat-field is also confirmed by the photometric results in the next section.

4.5 Photometry and Astrometry

Aperture photometry and astrometry was performed using `SEXTRACTOR`⁴ ([Bertin & Arnouts 1996](#)) and `SCAMP`⁵ ([Bertin 2006](#)), respectively. We set apertures with radii of 2, 4, 6 and 8 pixels (or arcsecs at our plate scale of $1''$ per pixel). As a compromise between bright and faint stars, we adopted the magnitude with an aperture radius of $4''$ as the default magnitude. In addition, we derived a Kron-like elliptical aperture magnitude `MAG_AUTO`, which is usually a robust estimator of total magnitude for galaxies. The windowed position was adopted to calculate the centroid, which has been shown to be as precise as a PSF-fitted position ([Becker et al. 2007](#)). To solve for the World Coordinate System, we adopt the Position and Proper Motions eXtended (PPMX, [Röser et al. 2008](#)) as the reference catalogue for its small size but high accuracy. The mean source density of PPMX is $\sim 440 \text{ deg}^{-2}$ and its typical 1-dimensional scatter is 40 mas. Therefore, with nearly 2000 reference stars with precise coordinates in a typical AST3-1 FoV, we can ensure accurate astrometric calibration. Our observed 1σ astrometric precision is $0''.1$ in both RA and DEC, while the internal precision reaches 40 mas for bright stars. This degree of precision with the astrometry is essential for image registration when using difference image analysis (DIA) for transient object detection.

4.6 Flux Calibration

We adopted the AAVSO Photometric All-Sky Survey (APASS⁶) DR9 catalogue ([Henden et al. 2016](#)) as the reference to calibrate AST3-1's magnitudes. APASS is an all-sky survey conducted in *BVgriz* filters. The *i*-band limiting magnitude reaches a depth of ~ 16 . Compared to the secondary *ugriz* standards ([Smith et al. 2002](#)), APASS *i* magnitude has a RMS scatter of 0.039 mag and no color trend ([Munari et al. 2014](#)). For the survey fields, we calibrate each frame to APASS. While for each monitored field, we only calibrate the frame with the best image quality to APASS and then adopt this frame as a reference to calibrate the others. The best frame is selected as the one with the most detected sources, which results from a combination of effects such as FWHM, sky brightness, dark current level and extinction.

⁴ <http://www.astromatic.net/software/sextractor>

⁵ <http://www.astromatic.net/software/scamp>

⁶ <https://www.aavso.org/apass>

When absolutely calibrating an image, we calculate the photometric offsets from instrumental to available APASS i magnitudes. The median offset of each frame was used as the zero point to calibrate the magnitude of all the sources in the frame. The left panel of Fig. 4 presents the offset from an example image (a0420.433.fit). Stars fainter than 14th magnitude exhibit larger dispersions due to the limited depth of APASS. Therefore, we only use 11–14 mag stars to derive the zero-point, which is 0.31 mag with a standard deviation of 0.06 mag in this example. A colour-free zero-point is applied since there was only one filter for AST3-1 in 2012. To investigate the effect of a colour term in the AST3-1 photometric calibration, we also compared the magnitude differences as a function of associated APASS $r - i$ colour, shown in the right panel of Fig. 4(b). The best linear fitting of the magnitude transformation is

$$i_{\text{AST3}} = i_{\text{APASS}} + 0.3(r - i)_{\text{APASS}} + 0.24.$$

Many factors contribute to the difference between two systems, including telescope throughput, CCD quantum efficiency and atmospheric transparency. The low water vapour contents of the atmosphere above Dome A results in significantly better transmission (Sims et al. 2012), which can affect the effective filter curves. The colour coefficient is as large as 0.3. Therefore caution should be taken when comparing AST3-1’s magnitudes with other surveys, especially for extremely blue or red targets. It is also critical when combining magnitudes from multiple facilities to derive the light curve of a colour-varying source. For example, tens of telescopes worldwide contributed to the observations of GW170817, the first optical counterpart of a gravitational wave event (Abbott et al. 2017). However, its $r - i$ colour varied from less than 0 to nearly 1 mag over four days. Consequently, large systematic errors of up to 0.3 mag can be induced in the light curve if no colour correction is applied between the various telescopes that are nominally observing in the same band.

In relative calibration for the same field, we find discernible position-dependent variations in magnitude differences between two frames. The reason is probably the variation of FWHM across the CCD and the application of a uniform size of aperture. Fig. 5 illustrates an example of Δ mag between a0410.316.fit and b0409.267.fit, which is the reference image in the field of HD 143414. The magnitude zero-point differs on the order of 0.02 mag across the CCD. To correct for this, we fitted a quadratic zero-point as a function of (X, Y) from using stars with $S/N > 50$, and adopt this to calibrate all the stars. This further reduces the observed scatter in the light curves for bright stars away from the CCD center compared to a constant zero-point. However, we do not apply the same correction in absolute calibration due to the insufficient accuracy of APASS.

5 PHOTOMETRIC ACCURACY

In order to estimate the photometric precision of single frame, we compared the magnitude differences between two images and illustrate with an example in Fig. 6. The results are based on two consecutive 60 s images a0330.104.fit and a0330.105.fit with FWHM $\sim 3''.7$. The upper panel shows the differences of aperture magnitude using a $2''$ radius and the

lower panel shows the 1σ deviation of magnitude difference in each 0.25 mag interval. Over-plotted solid lines indicate the photon noise of the signal and the background calculated for various apertures. The photon noise can be written as:

$$\sigma = 1.0857 \frac{\sqrt{(\pi r^2 S + F)/g}}{F},$$

where r is the aperture radius, S is the sky background, F is the source flux enclosed by the aperture r and g is the gain of CCD in electrons/ADU. Here we do not consider the read-out noise, which is negligible compared to the photon noise from the sky background. Nor do we include scintillation noise since its level is about 0.1 mmag (Kenyon et al. 2006), much is smaller than the photon noise of the brightest stars. Furthermore, we compare the precisions using aperture radii of 2, 4, 6, and $8''$.

As expected, smaller aperture provides more accurate measurements for the fainter range where the noise is dominated by sky background, while larger aperture is more suitable for bright stars where photon noise from the stars is dominant. For all apertures, the measured noise decreases when brighter and is almost identical to the photon noise in moderate magnitude range. However, it exceeds photon noise for bright stars, tending to be a constant regardless of decreasing photon noise, and starts to rise for stars brighter than $i \sim 11$, which are becoming saturated. The larger the aperture is, the smaller the deviation from photon noise. The constant noise is caused by systematic errors, including instability of the telescope and camera, variation of the atmospheric transparency and seeing, as well as residual errors from the flat-field and dark current corrections. In this example, the best 1σ precisions for four apertures are 10, 1.6, 1.1 and 0.8 mmag, respectively. By comparing with the photon noise it indicates that the systematic error is 10 mmag for aperture of $2''$, but is dramatically reduced to roughly 1 mmag for an aperture of $4''$ and is even negligible for aperture of $8''$. Since flux within a radius of $2''$ contributes to nearly half of the total flux, the systematic error would be reduced by a factor of 2 at most if little noise comes from annulus beyond $2''$. However, we observe a decrease by a factor greater than 10, which is likely a result of the difficulty in apportioning fluxes to fractional pixels in the $2''$ aperture. In summary, the stability of the AST3-1 system is much better than 1 mmag during the two minutes when these two images were taken.

At the faint end when $i > 18.5$, the measured error tends to be flat due to the lack of stars with Δ mag < 0 that are detected in one frame, but beyond the detection limit in the other frame. This selection bias results in the measured noise underestimating the real noise, so we take the photon noise to define the photometric depth. The $S/N = 5$ limiting magnitude is 18.7 with an aperture radius of $2''$ in this case.

These results demonstrate the capabilities of AST3-1 in both detection depth and photometric precision. A deeper detection limit would result from a sharper FWHM and lower sky background. For example, a FWHM of $2''.6$ in another image pair, a0331.116.fit and a0331.117.fit with similar sky brightness pushes the 5σ limiting magnitude down to $i \sim 19.3$. Here we remind the reader that although the seeing at Antarctic sites at a few meters above the boundary layer can be exceptional and reach values of $0''.3$, the surface see-

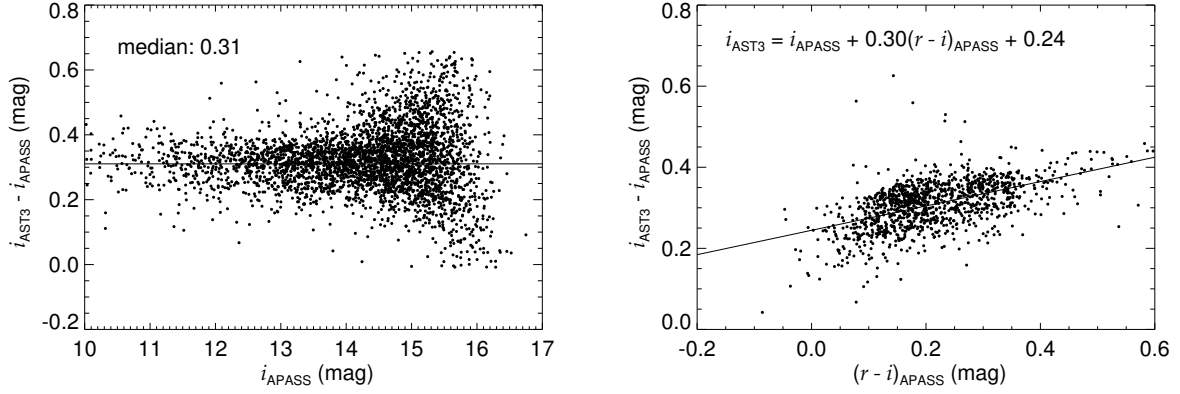


Figure 4. The difference between APASS i -magnitudes and AST3-1 instrumental magnitudes of 3,636 stars in an example frame a0420.433.fit as a function of (a) the APASS i -magnitudes shown in the left panel and (b) the APASS $r - i$ color for 1,207 stars with i_{APASS} between 11 and 14 shown in the right panel. The solid line in the left panel denotes the median value of the magnitude differences, which is adopted as the magnitude zero point. And the solid line in the right panel is the best linear fit to the colour dependence.

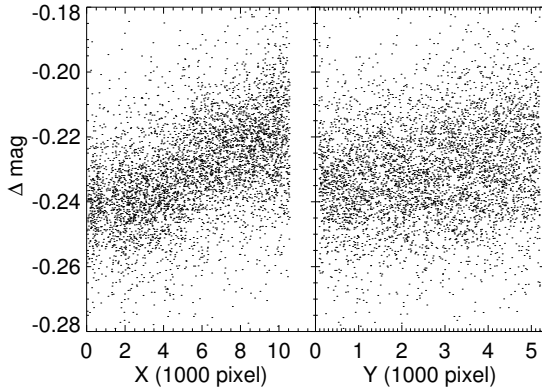


Figure 5. The obvious dependence of Δmag between b0409.267.fit and a0410.316.fit on CCD (X,Y) positions for 4,956 stars with $S/N > 50$.

ing is quite poor. For instance, the median seeing measured at the ground surface at Dome C is about $2''$ (Aristidi et al. 2009). On the other hand, the sky background in these examples is about $19.5 \text{ mag arcsec}^{-2}$ and would be one mag darker in a moonless polar night (Zou et al. 2010), which AST3-1 observations did not sample as a result of the power supply problem in early May 2012. Consequently, we infer that AST3 is able to approach a depth of $i \sim 20$ in a 60s exposure during dark nights under seeing-limited conditions within the turbulent boundary layer.

On the contrary, a sharper FWHM would degrade the photometric precision for bright stars. For example, the precision in an image pair of a0331.116.fit and a0331.117.fit is degraded to 2mmag. However, FWHM larger than $4''$ hardly improves the accuracy, which is usually dominated by systematic errors, but it extends the dynamic range to brighter stars. Therefore we can optimize the observational strategies for the transit survey mode according to the target magnitude ranges.

For long-term monitoring rather than just two contin-

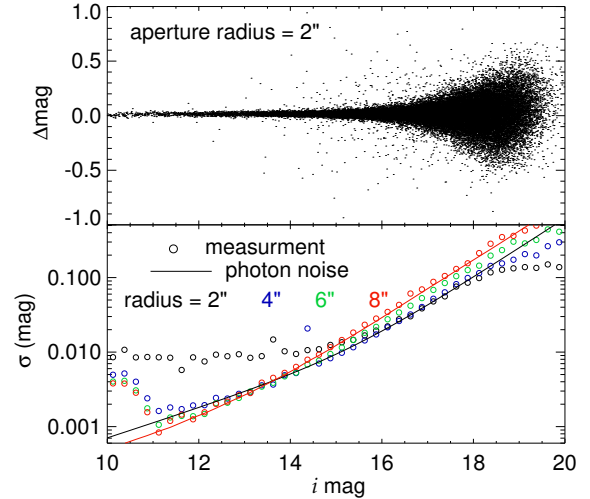


Figure 6. The upper panel presents the magnitude differences between two consecutive 60s exposures, a0330.104.fit and a0330.105.fit as a function of i -band magnitude, measured with a circular aperture of $2''$ in radius. The lower panel shows the RMS calculated in each 0.2-mag interval and different colors represent the results obtained for different aperture radii. Solid lines indicate the expected error from photon noise for different cases. The performance of the small aperture at the faint end shows a 5σ limiting magnitude of 18.7, while the precision from large apertures at the bright end reaches 0.8mmag, roughly the photon noise limit. It implies that the systematic error is indiscernible.

uous images, the systematic errors become predominant in light curves of bright stars, constraining the detection of tiny variabilities such as exoplanet transit signals. For instance, Fig. 7 shows a diagram of the RMS scatters in the light curves versus instrumental magnitude in the field centered on a Wolf-Rayet star HD 143414. This field was monitored on 8, 9, 10, 11 April and 5, 6 May for one to four hours on each night. We have obtained high-precision photometry with an RMS accuracy of $\sim 5 \text{ mmag}$ at the

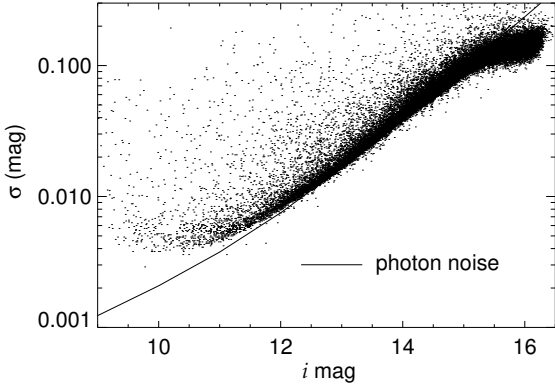


Figure 7. Typical dispersions for AST3-1 i -band light curves as a function of stellar brightness in field HD 143414. The solid line shows ideal photon noise under typical observing conditions. The RMS uncertainties for bright stars are limited to ~ 5 mmag due to systematic errors and relative calibration error.

bright end. We also present the theoretical photon-noise limit in a typical observing condition (an integration time of 10 s, a FWHM of $4''$, sky background of 1000 ADU due to full Moon and an extinction of 0.7 mag due to cloud or frost on the mirror). On account of these conditions, photon noise of the brightest stars is 2 mmag. The systematic errors arise from variations in exposure time, FWHM, sky brightness, transparency and position on CCD, as well as errors induced in image corrections and calibrations. The photometric accuracy may be further improved with more careful de-trending by those who are interested in these data. Similar result has been also obtained for the Transit field (see Fig. 1 in Wang et al. 2017), while for crowded fields such as the LMC-center, the photometric accuracy for bright stars is mainly limited by the difficulty of using aperture photometry on blended sources. To improve the precision, PSF photometry is desired and will be performed in the future.

In Fig. 8, we plot example light curves for HD 143414, one of our Wolf-Rayet star targets. The epoch of the observations are labeled. A photometric precision of better than 6 mmag is indicated by the scattering in the light curves of the comparison star, which is $210''$ away and ~ 0.8 mag fainter. The light curve of HD 143414 exhibits diverse variability on individual days and variabilities shorter than an hour are obvious. Detailed studies of stellar variabilities in the Transit field from the AST3-1 data set can be found in Wang et al. (2017).

Finally, we compared the AST3-1 photometry with the Southern Extension of $ugriz$ standard stars⁷ (Smith et al. 2007). This comparison enables a sanity check of the absolute photometric calibration of AST3-1 observations. The standards are located in a grid of fields spaced roughly every two hours of RA along Dec of -30° and -60° , as well as some special fields. Each field with $13'.5$ FoV contains dozens of standard stars with high photometric precision. There are

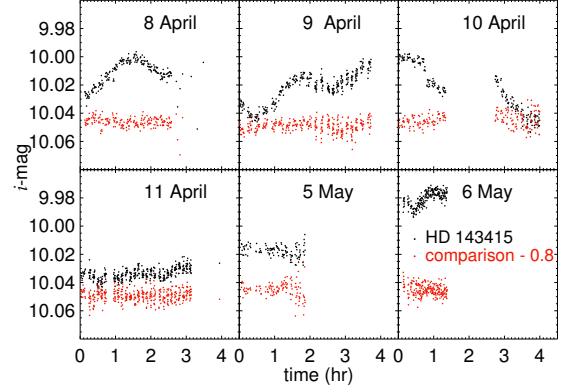


Figure 8. Light curves of HD 143414 (black dots) and a comparison star (red dots) on six days. Time zero denotes the first exposure of the star on each day. The magnitude RMS of the comparison star reaches 6 mmag, and HD 143414 exhibits obvious aperiodic variability on timescale of shorter than an hour.

six fields observed by AST3-1 in 2012, which are at $\alpha = 0^h, 2^h, 20^h, 22^h$ and $\delta = -60^\circ$, as well as the fields of JL 82 and NGC 458. The median magnitude differences between AST3-1 and the standard i system in these fields are $-0.03, -0.06, -0.01, -0.01, 0.00$ and -0.04 , respectively. This indicates that the absolute photometric calibration of AST3-1 has a RMS of about 0.02 mag. Besides, the $r-i$ colour coefficient in the i magnitude transformation is around 0.2 mag.

6 DATA ACCESS

The AST3-1 DR1 dataset is available to the community through the Chinese Astronomical Data Center⁸. The dataset consists of three parts: AST3-1 images, AST3-1 survey and AST3-1 light curves.

AST3-1 images includes 14,460 corrected images and corresponding catalogues from both the survey and monitoring observations, accompanied with observation information such as center coordinates, date, exposure time and image quality (see Table 3). The AST3-1 survey is a combined catalogue containing more than 16 million sources (see Table 1) down to $i \sim 19$ from the survey observations with positions and magnitudes (see Table 4). The mean values of positions and magnitudes are adopted for the stars detected in multiple images (the median number of observations is three). AST3-1 light curves also contains the sources from the monitored fields, as well as nearly 2 million light curves for the sources with more than 50 detections (see Table 2). Each light curve is presented as a PNG picture and available in multiple formats for download, including FITS binary table, CSV file and VOTable. Table 5 summarizes the relative information stored in the FITS header. In addition, we provide a tar file for each field containing all light curves in FITS, CSV and VOTable format, respectively (the link is at the top of the AST3-1 light curves webpage).

⁷ <http://www-star.fnal.gov/>

⁸ <http://explore.china-vo.org/>

Table 3. AST3-1 image Database Schema

| Column Name | Description |
|-------------|--|
| Field | Field name |
| IMAGE | Image name and download link |
| CATALOGUE | Catalogue name and download link |
| DATE-OBS | UTC time of the beginning of observation |
| MJD | Modified Julian date of the beginning of observation |
| EXPTIME | Integration time (s) |
| TEMP_CCD | Temperature of the CCD (K) |
| RA | Right Ascension J2000 of the image center (deg) |
| DEC | Declination J2000 of the image center (deg) |
| SKY | Background brightness (ADU) |
| FWHM | Median Full Width at Half Maximum across the FoV (pixel) |
| ELONGATION | Median ratio of semi-major to semi-minor axis across the FoV |

Table 4. AST3-1 survey Database Schema

| Column Name | Description |
|-------------|--|
| ID | Source index |
| RA | Right Ascension J2000 (deg) |
| DEC | Declination J2000 (deg) |
| MAG | Mean magnitude (mag) |
| MAGERR | Standard deviation of magnitudes (mag) |
| COUNT | Number of observations |

Table 5. AST3-1 light curve Table Schema

| Column Name | Description |
|-------------|---|
| DATE | UTC time of the beginning of observation |
| MJD | Modified Julian date of the beginning of observation |
| X | Windowed X position in CCD (pixel) |
| Y | Windowed Y position in CCD (pixel) |
| RA | Right Ascension J2000 (deg) |
| DEC | Declination J2000 (deg) |
| FLUX | Flux (ADU) |
| FLUX_ERR | Flux error (ADU) |
| MAG_AUTO | Magnitude in Kron aperture (mag) |
| MAGERR_AUTO | Magnitude error in Kron aperture (mag) |
| BACKGROUND | Background brightness (ADU) |
| FWHM | Full Width at Half Maximum, assuming a Gaussian profile (pixel) |
| A | Semi-major axis length (pixel) |
| B | Semi-minor axis length (pixel) |
| THETA | Position angle of semi-major axis (degrees East from North) |
| FLAGS | SExtractor flags for the source |
| R50 | Radii enclosing half of total flux |
| MAG | 4''-aperture magnitude (mag) |
| MAGERR | 4''-aperture magnitude error (mag) |

7 SUMMARY

In 2012, the first AST3 telescope, AST3-1, was deployed at Dome A in Antarctica to carry out time-domain surveys. During the commissioning phase, AST3-1 surveyed ~ 2000 deg² fields as well as the LMC and SMC, and monitored a dozen fields including the LMC center, a field for studying exoplanet transits and some Wolf-Rayet stars. After the raw data were returned to China, we performed aperture

photometry, calibrated the magnitudes and produced light curves in the monitored fields. In this paper we present the first data release, DR1, of the photometric data from the AST3-1 commissioning surveys. DR1 consists of 14 thousand scientific images, 16 million sources bright than $i \sim 19$ with photometry and astrometry, and 2 million light curves.

For faint sources, the 5σ limiting magnitude is $i \sim 18.7$ in 60 s with a typical FWHM of $3''.7$ and dramatically deepens to $i \sim 19.3$ with a sharper FWHM of $2''.7$. As a result,

we infer a depth of $i \sim 20$ in 60 s during a moonless night with FWHM of $2''$, which is the approximate median ground layer seeing. Along with its wide FoV, AST3-1 is capable of quickly discovering faint transients such as Near-Earth Asteroids, SNe and optical counterparts of GRBs and gravitational wave events. For example, the second AST3 participated in the follow-up of the first electromagnetic counterpart to a gravitational wave signal GW170817 and detected its quickly fading (Hu et al. 2017). At the bright end, ($i \approx 11$), AST3-1 achieved photon noise limited precision of 0.8 mmag, measured from two consecutive 60 s exposures. The AST3-1 photometry in light curves spanning one to two months is stable to a level of 5 mmag, mainly limited by variations in observational conditions and system stability. More careful de-trending and binning techniques can further reduce the systematic and statistical uncertainties. Therefore the dataset can be very useful in stellar variability research and the data in some fields are possible to be used for exoplanet detection. Moreover, our results provide suggestions for future strategies, such as choosing the integration time and FWHM for a given magnitude to optimize the precision.

In conclusion, the commissioning of AST3-1 has confirmed its promising prospects in time-domain astronomy, taking advantage of the clear and dark polar night at Dome A. The dataset from commissioning is public to the community through the Chinese Astronomical Data Center.

ACKNOWLEDGMENTS

The authors deeply appreciate the 28th and 29th CHINARE for their great effort in installing/maintaining AST3-1 and PLATO-A. This study has been supported by the National Basic Research Program (973 Program) of China (Grant No. 2013CB834900) and the Chinese Polar Environment Comprehensive Investigation & Assessment Program (Grant No. CHINARE2016-02-03), the National Natural Science Foundation of China (NSFC) (Grant Nos. 11403057, 11403048, 11203039 and 11273019). DWF and BLH acknowledge the support from NSFC (Grant No. 11503051), the Joint Research Fund in Astronomy (U1531115, U1731243) under cooperative agreement between the NSFC and Chinese Academy of Sciences (CAS), the National R&D Infrastructure and Facility Development Program of China, “Earth System Science Data Sharing Platform” and “Fundamental Science Data Sharing Platform” (DKA2017-12-02-XX). Data resources are supported by Chinese Astronomical Data Center (CAsDC) and Chinese Virtual Observatory (China-VO). S.W. thanks the Heising-Simons Foundation for their generous support. Y.Y. acknowledge the support from a Benozziyo Prize Postdoctoral Fellowship. ZHZ acknowledge the support from the 973 Program (Grant No. 2014CB845800), the NSFC (Grants Nos. 11633001 and 11373014), the Strategic Priority Research Program of the CAS (Grant No. XDB23000000) and the Interdiscipline Research Funds of Beijing Normal University.

The construction of the AST3 telescopes was made possible by funds from Tsinghua University, Nanjing University, Beijing Normal University, University of New South Wales, Texas A&M University, the Australian Antarctic Division and the National Collaborative Research Infrastructure Strategy (NCRIS) of Australia. It has also received

funding from the Chinese Academy of Sciences through the Center for Astronomical Mega-Science and National Astronomical Observatories (NAOC). This research was made possible through the use of the AAVSO Photometric All-Sky Survey (APASS), funded by the Robert Martin Ayers Sciences Fund.

REFERENCES

- Abbott, B. P., Abbott, R., Abbott, T. D., et al. 2017, *ApJ*, 848, L12
- Aristidi, E., Fossat, E., Agabi, A., et al. 2009, *A&A*, 499, 955
- Ashley, M. C. B., Bonner, C. S., Everett, J. R., et al. 2010, *Proc. SPIE*, 7735, 773540
- Bakos, G. Á., Csabry, Z., Penev, K., et al. 2013, *PASP*, 125, 154
- Bakos, G., Noyes, R. W., Kovács, G., et al. 2004, *PASP*, 116, 266
- Becker, A. C., Silvestri, N. M., Owen, R. E., Ivezić, Ž., & Lupton, R. H. 2007, *PASP*, 119, 1462
- Bellm, E. C. 2016, *PASP*, 128, 084501
- Bertin, E. 2006, *Astronomical Data Analysis Software and Systems XV*, 351, 112
- Bertin, E., & Arnouts, S. 1996, *A&AS*, 117, 393
- Bloemen, S., Groot, P., Woudt, P., et al. 2016, *Proc. SPIE*, 9906, 990664
- Bonner, C. S., Ashley, M. C. B., Cui, X., et al. 2010, *PASP*, 122, 1122
- Burton, M. G., Zheng, J., Mould, J., et al. 2016, *Publ. Astron. Soc. Australia*, 33, e047
- Chambers, K. C., Magnier, E. A., Metcalfe, N., et al. 2016, arXiv:1612.05560
- Chazelas, B., Pollacco, D., Queloz, D., et al. 2012, *Proc. SPIE*, 8444, 84440E
- Dong, S., Shappee, B. J., Prieto, J. L., et al. 2016, *Science*, 351, 257
- Drake, A. J., Djorgovski, S. G., Mahabal, A., et al. 2009, *ApJ*, 696, 870
- Godoy-Rivera, D., Stanek, K. Z., Kochanek, C. S., et al. 2017, *MNRAS*, 466, 1428
- Graham, M. J., Djorgovski, S. G., Stern, D., et al. 2015, *Nature*, 518, 74
- Henden, A. A., Templeton, M., Terrell, D., et al. 2016, *VizieR Online Data Catalogue*, 2336,
- Hu, L., Wu, X., Andreoni, I., et al. 2017, *Science Bulletin*, 62, 1433
- Hu, Y., Shang, Z., Ashley, M. C. B., et al. 2014, *PASP*, 126, 868
- Hu, Y., Shang, Z., Ma, B., & Hu, K. 2016, *Proc. SPIE*, 9913, 99130M
- Kaiser, N., Aussel, H., Burke, B. E., et al. 2002, *Proc. SPIE*, 4836, 154
- Kenyon, S. L., Lawrence, J. S., Ashley, M. C. B., Storey, J. W. V., Tokovinin, A., & Fossat, E. 2006, *PASP*, 118, 924
- Law, N. M., Kulkarni, S. R., Dekany, R. G., et al. 2009, *PASP*, 121, 1395
- Lawrence, J. S., Ashley, M. C. B., Tokovinin, A. & Travouillon, T. 2004, *Nature*, 431, 278
- Leloudas, G., Fraser, M., Stone, N. C., et al. 2016, *Nature Astronomy*, 1, 0002
- Li, Z., Yuan, X., Cui, X., et al. 2012, *Proc. SPIE*, 8444, 84441O
- Li, Y., Zheng, J., Tuthill, P., et al. 2016, *Publ. Astron. Soc. Australia*, 33, e008
- Liang, E.-S., Wang, S., Zhou, J.-L., et al. 2016, *AJ*, 152, 168
- Liu, Q., Wei, P., Shang, Z., et al. 2018, *Research in Astronomy and Astrophysics*, 18, 5
- Ma, B., Shang, Z., Hu, Y., et al. 2014, *Proc. SPIE*, 9154, 91541T
- Ma, B., Shang, Z., Wang, L., et al. 2012, *Proc. SPIE*, 8446, 84466R

- Margutti, R., Metzger, B. D., Chornock, R., et al. 2017, ApJ, 836, 25
- Meng, Z., Zhou, X., Zhang, H., et al. 2013, PASP, 125, 1015
- Munari, U., Henden, A., Frigo, A., et al. 2014, AJ, 148, 81
- Oelkers, R. J., Macri, L. M., Wang, L., et al. 2016, AJ, 151, 166
- Pollacco, D. L., Skillen, I., Collier Cameron, A., et al. 2006, PASP, 118, 1407
- Röser, S., Schilbach, E., Schwan, H., et al. 2008, A&A, 488, 401
- Saunders, W., Lawrence, J.S., Storey, J.W.V., Ashley, M.C.B., Kato, S., Minnis, P., Winker, D., Liu, G., Kulesa, C., 2009 PASP, 121, 976
- Shang, Z., Hu, K., Hu, Y., et al. 2012, Proc. SPIE, 8448, 844826
- Shappee, B. J., Prieto, J. L., Grupe, D., et al. 2014, ApJ, 788, 48
- Shi, S.-C., Paine, S., Yao, Q.-J., et al. 2016, Nature Astronomy, 1, 0001
- Sims, G., Ashley, M. C. B., Cui, X., et al. 2012, PASP, 911, 74
- Smith, J. A., Tucker, D. L., Kent, S., et al. 2002, AJ, 123, 2121
- Smith, J. A., Tucker, D. L., Allam, S. S., et al. 2007, *The Future of Photometric, Spectrophotometric and Polarimetric Standardization* (ASP Conf. Ser. 364), ed. C. Sterken (San Francisco: CA: ASP), 91
- Tonry, J. L. 2011, PASP, 123, 58
- Tonry, J. L., Denneau, L., Heinze, A. N., et al. 2018, arXiv:1802.00879
- Wang, L., Macri, L. M., Krisciunas, K., et al. 2011, AJ, 142, 155
- Wang, L., Ma, B., Li, G., et al. 2017, AJ, 153, 104
- Wang, S., Zhou, X., Zhang, H., et al. 2012, PASP, 124, 1167
- Wang, S.-H., Zhou, X., Zhang, H., et al. 2014, Research in Astronomy and Astrophysics, 14, 345-356
- Wang, S., Zhang, H., Zhou, J.-L., et al. 2014, ApJS, 211, 26
- Wang, S., Zhang, H., Zhou, X., et al. 2015, ApJS, 218, 20
- Wei, P., Shang, Z., Ma, B., et al. 2014, Proc. SPIE, 9149, 91492H
- Wheatley, P. J., West, R. G., Goad, M. R., et al. 2017, arXiv:1710.11100
- Yang, Y., Moore, A. M., Krisciunas, K., et al. 2017, AJ, 154, 6
- Yang, M., Zhang, H., Wang, S., et al. 2015, ApJS, 217, 28
- Yuan, X., Cui, X., Liu, G., et al. 2008, Proc. SPIE, 7012, 70124G
- Yuan, X., & Su, D.-q. 2012, MNRAS, 424, 23
- Zhou, X., Wu, Z.-Y., Jiang, Z.-J., et al. 2010, Research in Astronomy and Astrophysics, 10, 279
- Zong, W., Fu, J.-N., Niu, J.-S., et al. 2015, AJ, 149, 84
- Zou, H., Zhou, X., Jiang, Z., et al. 2010, AJ, 140, 602

This paper has been typeset from a $\text{\TeX}/\text{\LaTeX}$ file prepared by the author.